

LGL-BCI: A Lightweight Geometric Learning Framework for Motor Imagery-Based Brain-Computer Interfaces

1st Jianchao Lu

*School of Computing
Macquarie University
Sydney, Australia*

jianchao.lu@mq.edu.au

2nd Yuzhe Tian

*School of Computing
Macquarie University
Sydney, Australia*

yuzhe.tian@hdr.mq.edu.au

3rd Yang Zhang

*School of Computing
Macquarie University
Sydney, Australia*

yang.zhang@mq.edu.au

4th Jiaqi Ge

*College of Computer
Science and Technology
Jilin University
Jilin, China*

jiaqi.ge@mq.edu.au

5th Quan Z. Sheng

*School of Computing
Macquarie University
Sydney, Australia*

michael.sheng@mq.edu.au

6th Xi Zheng[§]

*School of Computing
Macquarie University
Sydney, Australia*

james.zheng@mq.edu.au

Abstract—Brain-Computer Interfaces (BCIs) are a ground-breaking technology for interacting with external devices using brain signals. Despite advancements, electroencephalogram (EEG)-based Motor Imagery (MI) tasks face challenges like amplitude and phase variability, and complex spatial correlations, with a need for smaller model size and faster inference. This study introduces the LGL-BCI framework, employing a Geometric Deep Learning Framework for EEG processing in non-Euclidean metric spaces, particularly the Symmetric Positive Definite (SPD) Manifold space. LGL-BCI offers robust EEG data representation and captures spatial correlations. We propose an EEG channel selection solution via a feature decomposition algorithm to reduce SPD matrix dimensionality, with a lossless transformation boosting inference speed. Extensive experiments show LGL-BCI's superior accuracy and efficiency compared to current solutions, highlighting geometric deep learning's potential in MI-BCI applications. The efficiency, assessed on two public EEG datasets and two real-world EEG devices, significantly outperforms the state-of-the-art solution in accuracy (82.54% versus 62.22%) with fewer parameters (64.9M compared to 183.7M).

Index Terms—Brain-Computer Interfaces (BCIs), Motor Imagery (MI), EEG Signal Processing, Geometric Deep Learning, Symmetric Positive Definite (SPD) Manifold

I. INTRODUCTION

Recent growth in electroencephalogram (EEG)-based Motor Imagery (MI) research, fueled by its transformative potential, has notably advanced Brain-Computer Interfaces (BCIs). BCIs provide a unique interface for individuals to control external devices using brain signals [1], significantly benefiting those with motor disabilities [2]. For example, paralyzed patients can use MI-BCIs to operate robotic limbs, communicate, and control computers.

Despite the rapid advancements in deep learning frameworks for EEG signal processing, MI-BCIs face enduring challenges such as: **(1) Variability to amplitude & phase.** Due to EEG signals' non-stationarity, making consistent extraction of these details difficult. Additionally, individuals can produce varying EEG signals under similar conditions, known as Inter-subject Variability. Even within a single individual, factors like fatigue or attention shifts can cause variations, known as Intra-subject Variability [3]. **(2) Complex spatial correlation.** The volume conduction effect causes signals from a specific brain area to be detected by multiple electrodes [4, 5], necessitating its mitigation for accurate EEG-based brain network analysis. Moreover, EEG data, being multi-dimensional from numerous scalp electrodes [6, 7], requires non-Euclidean techniques to retrieve spatial features relevant to MI-BCI, as opposed to traditional Euclidean-based methods [8, 9]. **(3) Model size & inference speed.** Effective MI-BCIs demand real-time operation, but large, complex deep learning models can cause latency, making them unsuitable for real-time use, especially in computationally constrained wearable BCI applications. Thus, it is essential to minimize model size and inference speed. This highlights the need for efficient neural network designs with rapid inference for optimal real-time performance [10].

Addressing these MI-BCI design challenges, we unveil LGL-BCI, a specialized framework optimized for MI tasks on resource-constrained devices, leveraging Geometric Deep Learning. While this framework also recommends non-Euclidean metric spaces like the SPD Manifold [11–13] for enhanced EEG representation, current methods suffer from model performance variability and high computational complexity, limiting mobile deployment. Our approach involves four modules: SPD manifold construction, spatial feature

[§]Corresponding Author

extraction within it, key EEG channel selection through a novel dimension reduction technique using geometry-aware mapping to tangent spaces, and employing CNN to extract temporal features from these spaces.

In a nutshell, our main contributions are threefold:

- **Pioneering Geometric Learning in EEG:** To the best of our knowledge, we are among the first to harness the Geometric Deep Learning Framework for EEG signal processing, utilizing the Symmetric Positive Definite (SPD) Manifold space for a robust EEG data representation.
- **Efficient LGL-BCI Framework:** Our LGL-BCI framework is tailored for MI tasks on resource-limited mobile devices, emphasizing reduced model size and swift inference speed without compromising accuracy.
- **Extensive Real-world Evaluations:** We validate our approach with comprehensive experimental studies, including evaluations on two public datasets and real-world collected data.

In the following of this paper, we will commence by providing background knowledge and motivations in Section II. Subsequently, we will present our LGL-BCI design in Section III. Following that, we will delve into the experimental design in Section IV and present a comprehensive discussion of the experimental results in Section V. Finally, we will provide some concluding remarks in Section VI.

II. BACKGROUND AND MOTIVATIONS

A. Geometric Deep learning

Riemannian Geometry learning elucidates curved spaces, notably the Symmetric Positive Definite (SPD) manifold, essential for EEG data analysis. Geodesics, the shortest paths between two points, are key in navigating these spaces. In the SPD manifold, the tangent space at a specific point is crucial, serving as a bridge between complex curvature and simple linear operations, thus simplifying EEG data interpretation [14].

B. Related Work

1) *Spatial Filtering Techniques and Their Limitations:* This school of research associates challenges with the signal-to-noise ratio (SNR) and has introduced various spatial filtering methods like Common Spatial Pattern (CSP) to improve SNR and amplify oscillatory brain activities pre-feature extraction [15–17]. However, the effectiveness of these techniques can be limited by feature extraction proficiency, particularly amid complex, event-driven, and unrelated neural oscillations [18].

2) *The Advent of CNNs in BCIs and Their Shortcomings:* Traditional deep learning methods like convolutional neural networks (CNNs) have proven effective in addressing the low SNR of EEG signals in the BCI domain [19–21]. Particularly, Motor Imagery-based BCIs aim to detect and interpret brain motor imagery patterns, with CNNs capturing temporal-spatial frequency features of neural signals, optimizing EEG data translation. However, due to structural differences between images and EEG signals, CNNs' feature expression in motor imagery tasks is hindered by the non-Euclidean nature of EEG signals [22–24]. To address this, we propose a geometric

learning-based Brain-Computer Interface, tackling not only the low SNR issue but also exploring the non-Euclidean relationships between EEG channels.

3) Utilizing Geometric Learning Approaches in MI-BCIs:

To handle non-Euclidean data structures effectively, geometric learning methods, mainly based on Riemannian geometry (RG), have been employed in MI-BCI [8, 25]. RG allows EEG data mapping onto a Riemannian manifold, yielding metrics resistant to outliers and noise [26]. It also addresses the “swelling effect” with larger determinant of Euclidean mean averaging from SPD matrices [27]. The manifold metrics exhibit invariance properties, enhancing model generalization for complex EEG signals [9]. Recent MI-BCIs [8, 28] primarily design the feature extraction module based on SPD manifolds using RG, where SPD matrices capture spatial correlations among EEG channels, crucial for understanding brain activity. These matrices, as Riemannian manifolds, possess specific invariance properties beneficial in practical applications, such as invariance under invertible linear transformations, useful for addressing amplitude & phase variability. However, operations with SPD matrices in MI-BCIs' signal feature extraction module see a complexity rise with increasing n (number of input signals), posing design challenges for large n MI-BCIs due to escalated storage ($O(n^2)$) and computational demands ($O(n^3)$) [25].

Addressing MI-BCI challenges, we introduce the Lightweight Geometric Learning Brain-Computer Interface (LGL-BCI). LGL-BCI trims input size, preserving inherent distance relationships through a geometry-aware transform. It also employs an unsupervised multi-bilinear transformation, bypassing manual labeling and aiding temporal feature extraction on the tangent space, enhancing computational efficiency without major information loss.

III. LGL-BCI DESIGN

In the LGL-BCI framework, we first introduce *BiMap*, transforming spatial covariance matrices within each frequency passband via $W \cdot X^{ij} \cdot W^T$, utilizing a full column-rank matrix W . Next, we use *Riemannian Batch Normalization*, a variant of conventional batch normalization for data on Riemannian manifolds, ensuring data stays within the manifold during training, aiding improved, accelerated convergence. We incorporate the *ReEig* layer as an activation function, akin to ReLU in traditional deep learning, rectifying input SPD matrices with a non-linear function applied to their elements or eigenvalues. Additionally, the *LogEig* layer maps SPD manifold elements to its tangent space, aiding in efficient processing as shown in Eq. 1:

$$\log(X_i) = U \text{diag}(\lambda_1, \dots, \lambda_d) U^T, \quad (1)$$

where $i = 1, \dots, d$, U is the orthogonal matrix of eigenvectors, and $\lambda_1, \dots, \lambda_d$ are the eigenvalues of X_i .

Building on previous SPD learning, we propose LGL-BCI. We first explain SPD manifold construction and spatial feature extraction from original signal data. Then, we detail our EEG Channel Selection Module for spatial dimension

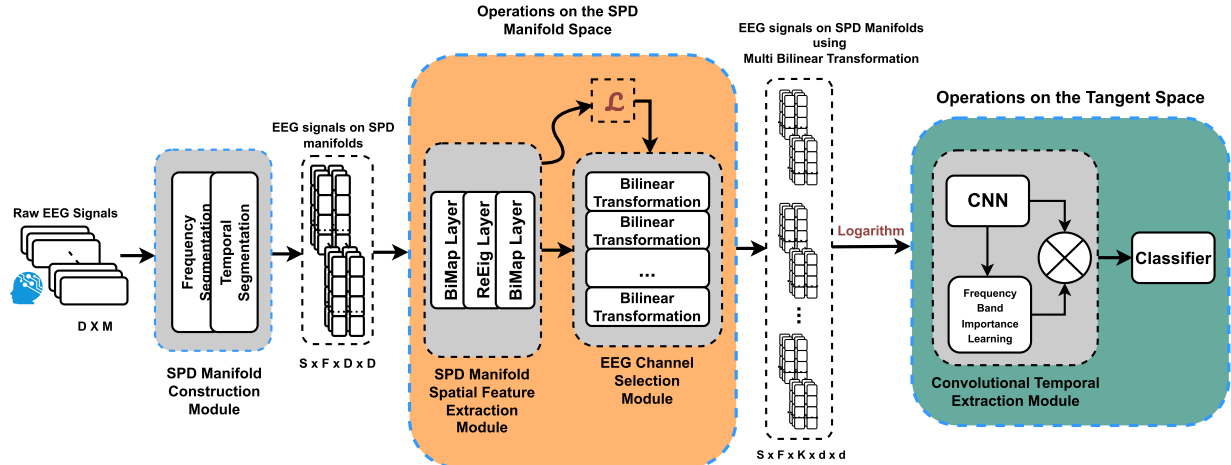


Fig. 1: Network Architecture of LGL-BCI

reduction while retaining SPD geometric properties. Finally, we introduce a temporal feature extraction module from the tangent space, employing the Multi-Bilinear transform and the *LogEig* layer.

A. SPD Manifold Construction Module

The SPD manifold construction module is responsible for transforming raw EEG data into SPD manifolds, acting as the ‘Signal Processing’ block in the LGL-BCI framework. This module receives multi-channel raw data from our data preprocessing pipeline, where the raw data is segmented both temporally and by frequency.

- (1) Frequency Segmentation: To segment the EEG signals in the frequency domain, we employ a well-known filter bank technique [29]. This technique uses a bank of bandpass filters to decompose the raw oscillatory EEG signals into multiple frequency passbands. We choose the causal Chebyshev Type II filter to ensure the non-negativity of filter coefficients and to minimize the filter transition bandwidth [8].
- (2) Temporal Segmentation: For temporal segmentation, we adopt a fixed-interval strategy. Initially, we divide the EEG signals into short, non-overlapping intervals of equal length. The length of each time window denoted as L , is determined based on Gabor’s uncertainty principle [30]:

$$\Delta t \cdot \Delta f \geq \frac{1}{4\pi}, \quad (2)$$

where Δt is the time width of the signal, and Δf is the frequency width of the signal. Gabor’s uncertainty principle states that time and frequency resolutions cannot be simultaneously maximized. This strategy ensures a balance between temporal and frequency resolutions of the EEG signals.

After frequency and temporal segmentation, we create four-dimensional tensors, $T \in \mathbb{R}^{S \times F \times M \times L}$, by stacking segments. Here, S , F , M , and L denote window slices, filter banks, channels, and window length, respectively. These tensors, T , help compute spatial covariance matrices, $X \in \mathbb{R}^{S \times F \times M \times M}$,

from EEG signals on SPD manifolds, serving as inputs for the spatial feature extractor module.

B. SPD Manifold Spatial Feature Extraction Module

The SPD Manifold Spatial Feature Extraction Module, designed to capture inherent spatial patterns in original Riemannian geometry, consists of a two-layer architecture acting like a specialized Multi-Layer Perceptron (MLP) for EEG signals on the SPD manifold. It contains the *BiMap* and *ReEig* layers, with *BiMap* functioning similarly to an MLP’s linear layer and *ReEig* acting as a non-linear spatial filter, enabling intricate spatial information extraction. The output is normalized using Riemannian Batch Normalization.

C. EEG Channel Selection Module

The EEG channel selection module involves identifying and choosing a subset of EEG channels that effectively capture the spatial patterns and structures present in EEG signals obtained from the previous module. The objective is to reduce the dimensionality of the SPD matrix from Sym_{++}^M to Sym_{++}^m where $M > m$ and retain the most important EEG channels. As the traditional channel selection methods in Euclidean space [31, 32] are not suitable in SPD manifolds, we develop a geometric-aware bilinear transformation to select critical EEG channels. The transformation is similar to *BiMap* from the RMTSISOM-SPDDR method [33] but adhere to the following key properties:

- (1) Preservation of Original SPD Data Points: Ensuring that data points remain on the SPD manifold after the transformation.
- (2) Maintaining Distances: Ensuring that the distances between data points in the tangent space after the transformation closely approximate their corresponding geodesic distances on the SPD manifold.

We will then describe how we construct the objective function based on these two properties to assist LGL-BCI in learning this transformation, thereby obtaining the most crucial EEG channels for specific MI tasks.

1) *Preservation of Original SPD Data Points*: Ensuring the preservation of original SPD data points is vital when transforming tangent vectors on the SPD manifold. To guarantee that the transformed vectors remain SPD, it is crucial to impose the constraint $W^T W = I_m$. This constraint ensures that the transformed tangent vectors remain as SPD and can be accurately mapped back to the manifold.

2) *Maintaining Distances*: There are two distances namely *Geodesic Distance* and *Euclidean Distance*. The set of SPD matrices Sym_{++}^m forms a Riemannian manifold. Hence, the geodesic distance between two SPD matrices X_i and X_j under the Affine Invariant Riemannian Metric (AIRM) [34], which is invariant to affine transformations, can be expressed as:

$$g_{ij} = \|\log(X_i^{-\frac{1}{2}} X_j X_i^{-\frac{1}{2}})\|_F, \quad 1 \leq i, j \leq N, \quad (3)$$

where $\|\cdot\|_F$ denotes the Frobenius norm. The tangent space is an Euclidean space. This allows for the computation of the Euclidean distance between tangent vectors. Specifically, for X_i and X_j from the SPD manifold, they are first mapped to its tangent space using the *LogEig* layer, resulting in the tangent vectors $\log(X_i)$ and $\log(X_j)$. These vectors, once transformed via the *BiMap* layer (i.e., $W^T \log(X_i)W$ and $W^T \log(X_j)W$), can have their distance computed as:

$$\begin{aligned} d_{ij} &= \|W^T \log(X_i)W - W^T \log(X_j)W\|_F \\ &= \|W^T (\log(X_i) - \log(X_j))W\|_F, \end{aligned} \quad (4)$$

Let $G = [g_{ij}]$ and $D = [d_{ij}]$ represent the Geodesic distance matrix and Euclidean distance matrix, respectively. To preserve the distances, it is expected that $G = D$.

3) *Objective Function for the Channel Selection*: To maintain the equality between Geodesic and Euclidean distance matrices, in our work, we design an objective function below to learn the optimal value of W in Eq. 4:

$$\begin{aligned} \hat{W} &= \arg \min_W \sum_{i=1}^N \sum_{j=1}^N (g_{ij} - d_{ij})^2 \\ &= \arg \min_W \|G - D\|_F^2 \quad (\text{Property 1}) \\ &\text{s.t. } W^T W = I_m \quad (\text{Property 2}) \end{aligned} \quad (5)$$

For $\forall g_{ij} \in G$ and $\forall d_{ij} \in D$, $(g_{ij} - d_{ij})^2 = g_{ij}^2 + d_{ij}^2 - 2g_{ij}d_{ij}$. Given that g_{ij} is expected to have a value very close to d_{ij} , the expression can be approximated as $g_{ij}^2 + d_{ij}^2 - 2g_{ij}d_{ij} \approx g_{ij}^2 + d_{ij}^2 - 2d_{ij}^2 = g_{ij}^2 - d_{ij}^2$. Then the Equation (5) can be rewritten as:

$$\begin{aligned} \hat{W} &= \arg \min_W \sum_{i=1}^N \sum_{j=1}^N (g_{ij}^2 - d_{ij}^2)^2 \\ &= \arg \min_W \|G^2 - D^2\|_F^2 \\ &\text{s.t. } W^T W = I_m \end{aligned} \quad (6)$$

Theorem 1. *If we let $A = (-\frac{1}{2}(G^2 - D^2))$, then HAH results in a Positive Semi-Definite (p.s.d) matrix, with $H = I_m - m^{-1}11^T$ representing the centring matrix. Here, $1 = [1, 1, \dots, 1]^T \in \mathbb{R}^m$, and I_m is a $m \times m$ identity matrix.*

Theorem 1 is derived from the Positive Semi-Definite Property [35] which states that: let $A = (-\frac{1}{2}z_{ij}^2)$, where z_{ij}^2 represents the Euclidean distance between i and j , then HAH is p.s.d. Here, we let $z_{ij}^2 \in (G^2 - D^2)$. Based on Theorem 1, we can center the objective function:

$$\begin{aligned} \hat{W} &= \arg \min_W \|H(-\frac{1}{2}(G^2 - D^2))H\|_F^2 \\ &= \arg \min_W \|\gamma_G - \gamma_D\|_F^2, \end{aligned} \quad (7)$$

Here, $\gamma_D = -\frac{1}{2}HD^2H$ and $\gamma_G = -\frac{1}{2}HG^2H$ are both p.s.d. It can be proven that both γ_D and γ_G are centred inner matrices [35], and we can obtain:

$$d_{ij}^2 = (\gamma_D)_{ii} + (\gamma_D)_{jj} - 2(\gamma_D)_{ij} \quad (8)$$

Moreover, base on the definition of Frobenius inner product, \hat{W} can be further rewritten as:

$$\hat{W} = \arg \min_W [-2\text{tr}(\gamma_G \gamma_D^T)] + \|\gamma_G\|_F^2 + \|\gamma_D\|_F^2. \quad (9)$$

Since $d_{ij} = \|W^T(\log(X_i) - \log(X_j))W\|_F$ (Eq. 4) and let $k_{ij} = \|X_i - X_j\|_F$, it follows that $d_{ij} \leq k_{ij}$. Also, $\gamma_D = -\frac{1}{2}HD^2H$ (Eq. 7), $\gamma_K = -\frac{1}{2}HK^2H$, thus $\|\gamma_D\|_F^2 \leq \|\gamma_K\|_F^2$. Let

$$\hat{W}^* = \arg \min_W [-2\text{tr}(\gamma_G \gamma_D^T)] + \|\gamma_G\|_F^2 + \|\gamma_K\|_F^2. \quad (10)$$

Hence, \hat{W} satisfies a specific inequality: $\hat{W} \leq \hat{W}^*$.

This inequality gives us an upper bound for the objective function. Besides, since $\|\gamma_G\|_F^2$ and $\|\gamma_K\|_F^2$ are unrelated to W , thus \hat{W} can be rewritten as:

$$\begin{aligned} \hat{W} &= \arg \min_W (-2\text{tr}(\gamma_G \gamma_D^T)) \\ &= \arg \min_W (-2 \sum_{i=1}^N \sum_{j=1}^N (\gamma_D)_{ij} (\gamma_G)_{ij}) \end{aligned} \quad (11)$$

Let $\theta_i = W \log(X_i)W$ and $\theta_j = W \log(X_j)W$ and from Equation (8), we can have:

$$2\gamma_{D_{ij}} = \|\theta_i\|_F^2 + \|\theta_j\|_F^2 - \|\theta_i - \theta_j\|_F^2 \quad (12)$$

Substitute Equation (12) into Equation (11), we have:

$$\hat{W} = \arg \min_W (\|\theta_i - \theta_j\|_F^2 (\gamma_G)_{ij}) \quad (13)$$

Accordingly, the objective function for the EEG Channel Selection Module can be formulated as:

$$\hat{W}_{t+1} = \text{argmax } \text{tr}(W^T \mathcal{L} W) \quad \text{s.t. } W^T W = I_m \quad (14)$$

Here, \mathcal{L} is defined as follows:

$$\mathcal{L} = - \sum_{i=1}^N \sum_{j=1}^N (\gamma_G)_{ij} \underbrace{(\log(X_i) - \log(X_j)) \hat{W}_t \hat{W}_t^T (\log(X_j) - \log(X_i))^T}_{\mathcal{F}(D)} \quad (15)$$

The expression \mathcal{L} comprises functions of G and D , denoting a unique link between the geometric and Euclidean distances among EEG channels. By conducting an eigenvalue decomposition on \mathcal{L} , we unveil the importance of corresponding eigenvectors in the transformation, employing the indices of the top d eigenvectors to discern the most significant d channels.

4) *Multi Bilinear Transformation*: The EEG Channel Selection Module picks top d features from data using eigenvalues, but may miss crucial information in unselected channels. To address this, we propose the Multi Bilinear Transformation (MBT), taking inspiration from Vaswani et al.’s multi-head attention mechanism [36]. MBT employs K bilinear transformations to explore distinct spatial correlations among top d channels, enabling the uncovering of K diverse spatial correlations. Unlike standard multi-head attention which concatenates single heads from varying representation subspaces, our mechanism stacks individual signal heads, forming a multi-channel feature map with each channel depicting a distinct signal head:

$$MBT = \text{Stack}(\text{head}_1, \text{head}_2, \dots, \text{head}_K) \quad (16)$$

D. Convolutional Temporal Extraction Module

In LGL-BCI, CNNs are employed to capture EEG signals’ temporal dynamics on the tangent space by reshaping the EEG Channel Selection Module output. The reshaping is from $\mathbb{R}^{(S \times F \times K) \times m \times m}$ to $\mathbb{R}^{F \times 1 \times S \times (K \times m \times m)}$, excluding the SPD structure. Here, F , S , K , and m denote frequency bands, window slices, multi-bilinear transformation, and the dimension of outputs respectively. Utilizing a 2D CNN, the temporal dynamics are captured, and through Riemannian geometry’s context, the classification problem transfers from manifold domain to Euclidean domain using the logarithm map. The 2D CNN, with a kernel width of $S \times (K \times m \times m)$, encompasses all chosen channels in one kernel, minimizing EEG electrodes’ spatial position impact. The CNN isn’t applied to the frequency band dimension, acknowledging varying contributions to MI tasks. A frequency band importance learning block is defined as follows to weigh significant bands:

$$\mathcal{E} = \sigma_2(\omega_2(\sigma_1(\omega_1(\mathcal{F}_{sq}(\mathcal{O}))))). \quad (17)$$

Here, \mathcal{O} is the output of the 2D CNN, $\omega_1 \in \mathbb{R}^{m \times \frac{m}{2}}$ and $\omega_2 \in \mathbb{R}^{\frac{m}{2} \times m}$ represent a two-layer fully connected neural network, σ_1 is a Relu activation function and $\mathcal{F}_{sq}(\mathcal{O})$ is a squeeze operation [37]:

$$\mathcal{F}_{sq}(\mathcal{O}) = \frac{1}{m \times m} \sum_{i=1}^m \sum_{j=1}^m (\mathcal{O}_{ij}). \quad (18)$$

The Sigmoid function, denoted as σ_2 , is used to evaluate the channel importance. This choice is motivated by the fact that multiple channels can contribute simultaneously and independently to the overall MI classification tasks, allowing for a flexible and distributed representation of frequency band importance. Finally, \mathcal{O} is updated accordingly:

$$\mathcal{O} = \mathcal{E} \times \mathcal{O}. \quad (19)$$

IV. EXPERIMENTAL DESIGN

In this section, we first present the three research questions of this study. Subsequently, we provide detailed introductions to the experiment setups for investigating these three research

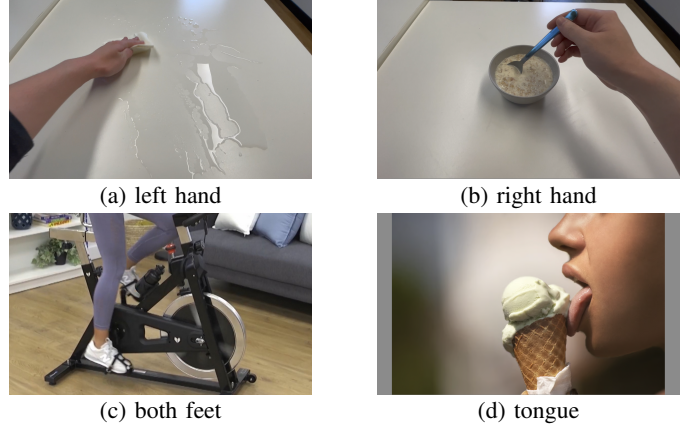


Fig. 2: Images for signifying motor imagery tasks.

questions. We formulate three research questions as the following:

- **RQ1:** How does LGL-BCI’s generalization capability perform on EEG-based motor imagery tasks?
- **RQ2:** How does LGL-BCI work within a real-world motor imagery setting?
- **RQ3:** How does the LGL-BCI framework generalize when utilized with a different EEG device?

A. Experimental Setup

1) *Setup for RQ1*: We evaluate LGL-BCI’s generalization using two public MI datasets: MI-KU [38] and BCIC-IV-2a [39]. MI-KU has 54 participants in a binary-class MI task, recorded via 62 electrodes at 1,000 Hz, with two sessions of 200 trials each. BCIC-IV-2a features nine subjects in a four-class MI-EEG task, recorded via 22 electrodes and three EOG channels at 250 Hz, with training and evaluation sessions comprising six runs of 12 trials for each class, totaling 288 trials per subject. LGL-BCI is benchmarked against several baseline techniques including CSP-based (FBCSP [29]), Riemannian-based approaches (MDM[40] / TSM[41] / SPDNet[25] / Tensor-CSPNet[8] / Graph-CSPNet[42]), and traditional deep learning methodologies (ConvNet[43] / EEGNet[18] / FBCNet[44]), showing its generalization capabilities.

2) *Setup for RQ2*: We evaluate LGL-BCI on a custom dataset from 20 participants, equally split by gender, with a mean age of 23 within a 20-25 age range. They perform four motor imagery tasks involving imagining movements of the *left hand*, *right hand*, *both feet*, and *tongue*, as shown in Fig. 2, chosen for their proven efficacy in stimulating different brain regions [45]. Seated 2 meters from a 27" monitor, they are cued by a visual and auditory signal to start a task, continuing until the visual cue disappears (around 10 seconds). The study contains six runs with 40 trials each, totaling 60 repetitions per task, with 3 to 5-minute breaks between runs to deter adaptation. Each run’s tasks are randomized.

The EEG data from participants is captured using OpenBCI Ultracortex Mark IV 16-channel EEG Cap [46] (as shown



Fig. 3: Photos of different hardware sets

in Fig. 3a), with real-time data collection via the OpenBCI API, sampled at 128 Hz. LGL-BCI is run on a local desktop, processing the transmitted EEG data for Motor Imagery (MI) classification. During training, cross-entropy is chosen as the loss function for its simplicity, with a batch size of 64 and learning rate of $1e^{-3}$. Training occurs over 100 epochs on an NVIDIA GeForce RTX 4090 GPU.

3) *Setup for RQ3 LGL-BCI's experimental setup with a new EEG device:* The usage of a different EEG system, Emotiv EPOC Flex¹ (as shown in Fig. 3b), alongside Emotiv Cortex API for data reading, helps in evaluating LGL-BCI's generalization capability. Given the variation in EEG data values from this hardware compared to the previous one, it serves as a test for LGL-BCI's adaptability. All other settings remain as per RQ2.

V. EXPERIMENTAL RESULTS

In this section, we present detailed experimental results in response to the research questions we previously highlighted.

A. Result Analysis of RQ1 – Comparative Analysis: LGL-BCI Generalization Performance vs. Leading-Edge Methodologies

Comparison with Other Leading-Edge Methods: To assess the generalization capabilities of LGL-BCI, we compared it with the currently popular methods for handling MI tasks on the MI-KU and BCIC-IV-2a datasets. These datasets are designed around three separate scenarios—two using a 10-fold-cross-validation (CV) technique and one incorporating a holdout scenario. The performance metrics of various methodologies are detailed in Table I.

The conventional deep learning (DL) method for MI-EEG classification relies on leveraging the temporospatial frequency characteristics of EEG signals. Both EEGNet and ConvNet utilize these patterns, achieving performance metrics comparable to FBCSP, a known strategy for extracting temporospatial frequency patterns. This performance equivalence suggests that integrating any two components can markedly enhance the classification process. FBCNet, drawing on temporospatial frequency patterns, surpasses EEGNet and ConvNet across all scenarios, primarily attributed to the employment of bandpass filters adept at capturing frequency information.

The discussion transitions to Riemannian-based models, where MDM and TSM methods employ geodesic distances and projected SPD matrices on the tangent space of (Sn++,

AIRM) respectively for EEG classification. As Table I displays, their performance on the MI-KU dataset is akin to random guessing, though a slight enhancement is observed on the BCIC-IV-2a dataset. Despite SPDNet introducing a fresh approach for deep non-linear learning on SPD matrix Riemannian manifolds, it trails all other Riemannian-based models and DL methodologies in Table I. The outcomes of MDM, TSM, and SPDNet underline the limitations of employing geometric quantities of SPD manifolds for high-level classification features.

A notable performance elevation is attained with Riemannian-based models in Tensor-CSPNet and Graph-CSPNet, especially Graph-CSPNet, which marginally excels in nine out of eleven scenarios. This superior performance is largely credited to its refined time-frequency segmentation technique, offering a more accurate EEG signal characterization. With a streamlined parameter count, LGL-BCI approaches state-of-the-art results, a milestone reached by its capacity to discern and select the most pivotal channels. This not only minimizes the learnable parameter size but also enhances its efficacy in pinpointing the most crucial frequency bands.

Table II presents a performance comparison on the BCIC-IV-2a dataset among Tensor-CSPNet, Graph-CSPNet, and LGL-BCI. LGL-BCI displays an accuracy increment of around 2% over Tensor-CSPNet (76.95% vs. 75.11%), while cutting down the parameter count by nearly 130M (100.5M vs. 232.3M). Although LGL-BCI's accuracy is slightly below Graph-CSPNet's by about 1% (76.95% vs. 77.55%), it achieves this outcome with a significant parameter reduction of about 70M (100.5M vs. 169.4M).

To further scrutinize and evaluate the model's performance, we carry out additional ablation studies and visualizations based on the BCIC-IV-2a dataset below.

Influence of Varied Channel and Head Selection on LGL-BCI Efficacy: According to Table III, it aligns well with common sense that the performance of the model improves as the number of EEG channels used increases. Interestingly, we also observed that as the number of selected channels decreases, the model's accuracy does not show a significant decline. Notably, even with a decrease in the number of channels from 20 to 5, the model still achieves a comparatively high accuracy. This finding highlights the effectiveness of our channel selection module in accurately identifying the important channel contributions to the MI task.

Our proposed channel selection mechanism adeptly mitigates computational complexity by strategically omitting less significant channel information, which in turn reduces the dimensionality of the SPD matrix, all while maintaining the model's precision. Yet, we harbor the ambitious aspiration of enhancing the model's performance, even in the face of the loss of some less critical channel information. Drawing inspiration from the ingenious design of multi-head attention, we have crafted a multi-head-based subspace mapping method. While this approach indeed increases the number of heads, it also allows for a proportional reduction in the size of each

¹<https://www.emotiv.com/product/epoc-flex-saline-sensor-kit/>

TABLE I: Comparative Analysis of Subject-Specific Accuracies and Standard Deviations in MI-KU and BCIC-IV-2a Datasets.

MI-KU			BCIC-IV-2a			
	CV (S1) %	CV (S2) %	Holdout (S1 → S2) %	CV (T) %	CV (E) %	Holdout (T → E) %
FBCSP [29]	64.33 (15.43)	66.20 (16.29)	59.67 (14.32)	71.29 (16.20)	73.39 (15.55)	66.13 (15.54)
EEGNet [18]	63.35 (13.20)	64.86 (13.05)	63.28 (11.56)	69.26 (11.59)	66.93 (11.31)	60.31 (10.52)
ConvNet [43]	64.21 (12.61)	62.84 (11.74)	61.47 (11.22)	70.42 (10.43)	65.89 (12.13)	57.61 (11.09)
FBCNet [44]	73.36(13.71)	73.68(14.97)	67.74(14.52)	75.48 (14.00)	77.16 (12.77)	71.53 (14.86)
MDM [40]	50.47 (8.63)	51.93 (9.79)	52.33 (6.74)	62.96 (14.01)	59.49 (16.63)	50.74 (13.80)
TSM [41]	54.59 (8.94)	54.97 (9.93)	51.65 (6.11)	68.71 (14.32)	63.32 (12.68)	49.72 (12.39)
SPDNet [25]	57.88 (8.68)	58.88 (8.68)	60.41 (12.13)	65.91 (10.31)	61.16 (10.50)	55.67 (9.54)
Tensor-CSPNet [8]	73.28 (15.10)	74.16 (14.50)	69.50 (15.15)	75.11 (12.68)	77.36 (15.27)	73.61 (13.98)
Graph-CSPNet [42]	72.51 (15.31)	74.44 (15.52)	69.69 (14.72)	77.55 (15.63)	78.82 (13.40)	71.95 (13.36)
LGL-BCI ^(20,4)	72.56 (14.33)	73.90 (14.7)	69.10 (14.52)	76.95 (12.41)	77.13 (12.17)	73.69 (12.14)

TABLE II: Performance comparison and parameter efficiency in BCIC-IV-2a among Tensor-CSPNet, Graph-CSPNet, and LGL-BCI.

Method	Parameters (10M)	Accuracy (%)
Graph-CSPNet	16.94	77.55
LGL-BCI	10.05	76.95
Tensor-CSPNet	23.23	75.11

TABLE III: Impact of channel selection on model performance in head 1 and head 4 settings.

Channel No.	Accuracy (%) - Head 1	Accuracy (%) - Head 4
20	73.93	76.95
15	73.37	75.74
10	69.83	73.74
5	65.02	72.18

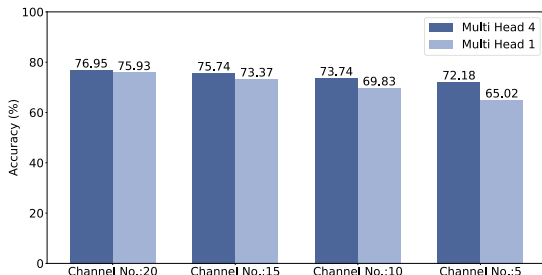


Fig. 4: Evaluating the performance differential across various channels selected in head 1 and head 4 settings.

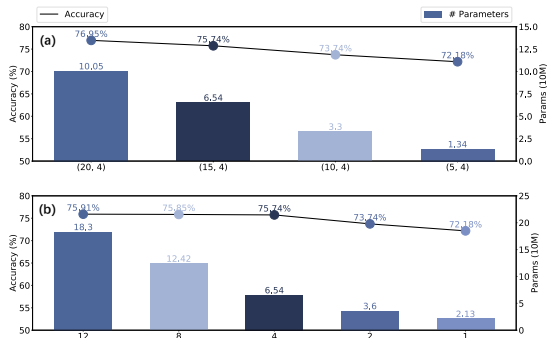


Fig. 5: Analyzing trade-offs between cost and accuracy: a comparison of channel selection and multi-head number choice.

head—that is, the dimension of the respective subspaces.

Figure 4 provides a comparative analysis of the performance

of various models with different channel counts, both before and after implementing the multi-head solution. The analysis reveals a consistent improvement in the performance of models that employ the multi-head solution. Interestingly, when all 20 channels are employed, the performance boost observed post-application of the multi-head solution is less noticeable. This implies that the use of the full channel spectrum can encapsulate most of the pertinent information necessary for the classification of MI tasks, whether the multi-head is utilized or not. However, when only the most critical K channels are used for MI tasks (such as when 15, 10, and 5 channels are selected), the multi-head solution serves as a compensatory mechanism to account for the loss of less essential channel information. The findings indicate that the fewer channels selected, the greater the potential for accuracy improvement. For instance, when 15 channels are selected, the multi-head solution boosts accuracy by 2%, while a significant improvement of over 7% occurs when only 5 channels are selected. These results demonstrate the multi-head solution's capability to enhance the model's learning efficiency and representation of the complex interplay between the manifold and its tangent space mapping, thus improving overall performance.

Figure 5 provides a comparison of cost and accuracy achieved across different numbers of channels and heads. With a constant number of heads, as shown in Figure 5 (a), reducing the channel number (from 20 to 5 channels) significantly decreases the parameters (from 100.5M to 13.4M), but the accuracy experiences a minimal decrease (from 76.95% to 72.18%). This indicates that our proposed model can effectively select the most critical channels representing useful EEG signals. Conversely, with a constant number of channels, as the number of heads increases (from 1 to 12), accuracy continues to increase, albeit at a decelerating rate (as shown in Figure 5 (b)). A balancing point can be found at (15, 4), where the accuracy increase begins to slow, and the parameter size is relatively low. This analysis provides insights on how to balance model performance between cost and accuracy.

Figure 6 illustrates the unique feature distributions for each of the four heads across all four MI tasks. Each distribution comprises 648 samples, and four (left hand, right hand, and both feet) to five (tongue) distinct clusters can be observed for each head in every task. This is indicative of the ability of our proposed multi-head-based subspace mapping method

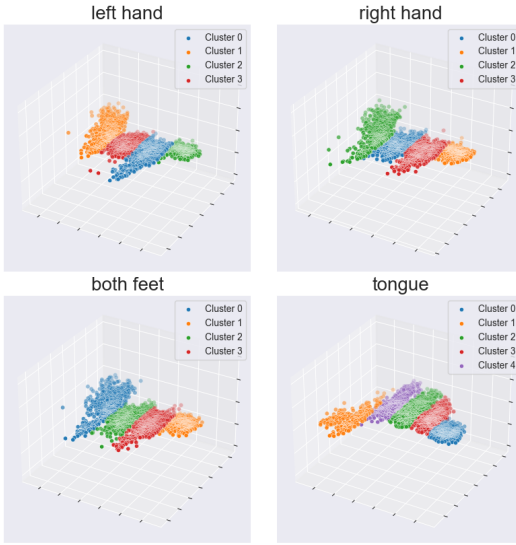


Fig. 6: Visualizing the distribution of feature representations across four motor imagery tasks from four heads. The visualization incorporates feature data from a total of 2,592 samples, with each MI task contributing 648 samples. In order to create a three-dimensional map, all the features from various heads are amalgamated and processed through Principal Component Analysis (PCA). Subsequently, the quality of the clustering is assessed utilizing the silhouette score.

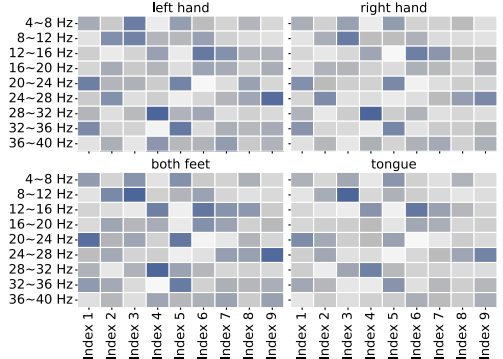


Fig. 7: Significance heatmap of frequency bands across four MI tasks.

to enhance feature diversity within the latent space. This diversity, in turn, facilitates a more comprehensive exploration of the tangent space while simultaneously capturing additional spatial information.

Frequency Band Importance Learning: Through the study of nine frequency bands, we discern the significance of these bands across four Motor Imagery (MI) tasks, as illustrated in Figure 7. In general terms, the importance distribution of these frequency bands shows a remarkable similarity across the four MI tasks. In this context, Index 1 signifies the frequency band(s) that the model customarily identifies as most vital. Conversely, Index 9 denotes the frequency band(s) the model typically views as least significant. A deeper analysis of the chart content leads to the following findings:

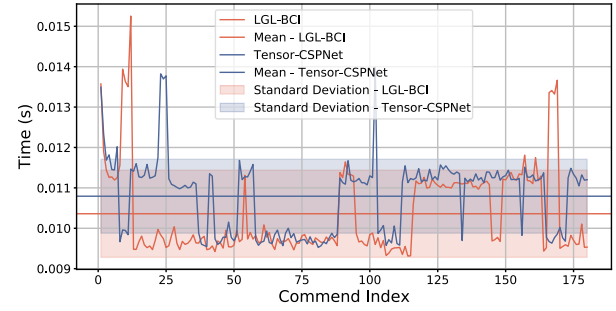


Fig. 8: Comparative Analysis of Inference Speed: LGL-BCI vs. Tensor-CSPNet.

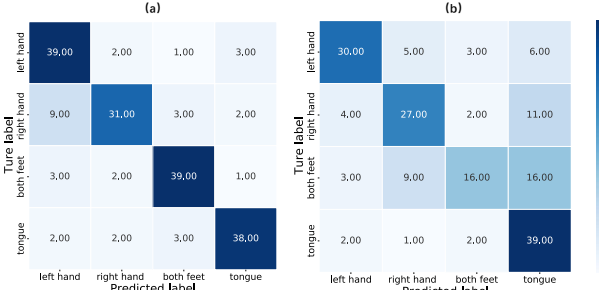


Fig. 9: Comparative confusion matrices illustrating MI classification performance: (a) LGL-BCI and (b) Tensor-CSPNet.

- (1) In the *left hand movement* task, the model generally focuses on the 20Hz-24Hz and 32Hz-36Hz bands at Index 1, along with the 24Hz-28Hz band at Index 2. A similar pattern is observable in the *right-hand movement* task, which makes sense considering both tasks fundamentally involve the imagined motion of the hand.
- (2) For the *both-feet movement* and *tongue movement* tasks, the model typically assigns more focus to the 20Hz-24Hz band. At Index 2, the model dedicated to the *both-feet movement* task usually gives more attention to the 8Hz-12Hz band, while the model for the *tongue movement* task does not typically show notable attention to any specific frequency band.
- (3) At Index 3, the model for the *tongue movement* task often gives the most attention to the 8Hz-12Hz band out of all indices from 1 to 20. This suggests that for most samples, the 8Hz-12Hz band is usually seen as particularly informative, even if it is not the most important band (Index 1). Indeed, this observation at Index 3 is not limited to the *tongue movement* task. Across all four MI tasks, the 8Hz-12Hz band is often considered important at Index 3.

By studying the significance of frequency bands, the performance of our model typically improves by approximately 2%, while also generally enhancing the model's interpretability.

B. Result Analysis: RQ2 – Performance of LGL-BCI on Custom Real-World Dataset

We embark on the evaluation by meticulously examining the performance of LGL-BCI on Custom Real-World Dataset.

TABLE IV: Comparison of performance, parameter efficiency, and response time between Tensor-CSPNet and LGL-BCI in motor imagery tasks.

Method	Parameters (10M)	Accuracy (%)
LGL-BCI	6.49	82.54
Tensor-CSPNet	18.37	62.22

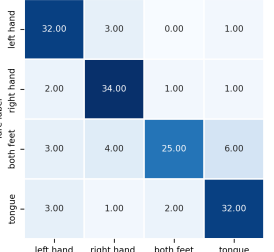


Fig. 10: Performance of LGL-BCI on Emotiv headset.

For comparative insight, we juxtapose this with the results produced by Tensor-CSPNet. Tensor-CSPNet, credited as the trailblazer of the geometric deep learning (GDL) paradigm in the field of MI-EEG classification, skillfully utilizes deep neural networks in tandem with the SPD manifolds to sequentially unravel EEG patterns across the spectrum of frequency, space, and time domains. Given that LGL-BCI aligns with a similar signal preprocessing approach and is also architected based on the SPD manifold, Tensor-CSPNet is a fitting benchmark to evaluate the prowess of LGL-BCI in the same scenarios. We involve three independent individuals who have not previously participated in the data collection process. They are assigned to perform the four random motor imagery tasks in a random order. As visually represented in Table IV, LGL-BCI surpasses Tensor-CSPNet in terms of accuracy, achieving 82.54% compared to Tensor-CSPNet's 62.22%. Remarkably, it accomplishes this with fewer parameters (64.9 M versus Tensor-CSPNet's 183.7 M). Furthermore, we examine the inference speed of both LGL-BCI and Tensor-CSPNet, as illustrated in Figure 8. Our findings reveal that LGL-BCI offers a substantially faster average inference speed than that of Tensor-CSPNet.

To delve deeper into the performance of both LGL-BCI and Tensor-CSPNet predictions, we compile confusion matrices for a more granular view (as shown in Figure 9). Among the set of 180 commands, LGL-BCI accurately predicts 147, thus achieving an accuracy rate of around 82%. This significantly trumps the accuracy demonstrated by Tensor-CSPNet. Upon more intricate inspection, we find that LGL-BCI sporadically misinterprets the 'left hand' and 'right hand' commands, with nine instances of 'right hand' wrongly identified as 'left hand' and two instances of the inverse situation. A comparative analysis of the confusion matrices from LGL-BCI and Tensor-CSPNet illuminates this discrepancy, indicating that such misinterpretations occur less frequently with LGL-BCI. Moreover, the commands for 'both feet' and 'tongue' register higher accuracy rates, thereby underscoring LGL-

BCI's proficiency in translating motor imagery recognition into distinct control commands with commendable accuracy. This aptly reflects its pragmatic potential in managing real-world devices.

C. Result Analysis: RQ3 – Real World Experimental Results

At current stage, there are no international standards nor de facto standards on the market. This situation will inevitably lead to differences in the output data between products from different suppliers, due to different designing, manufacturing, and software supporting. For instance, the values of the EEG data provided by Emotiv EPOC Flex is drastically different from that provided by OpenBCI Ultracortex.

To explore the performance of LGL-BCI on different devices, we perform an extra, small scale experiment with the Emotiv EPOC Flex headset. After gathering data from two participants (one male and one female) with Emotiv headset, we use the gathered data to fine-tune the pre-trained LGL-BCI model from RQ2. After fine-tuning, the accuracy can still reach 82%, the confusion matrix is also shown in Fig. 10. This experiment indicates that our LGL-BCI can perform well even if the hardware has changed to a model which outputs different range of EEG data value.

VI. CONCLUSION

Brain-Computer Interfaces (BCIs) stand as a transformative advancement, bridging human cognition with external devices. Even with notable strides, EEG-based Motor Imagery (MI) continues to confront obstacles such as amplitude and phase inconsistencies, intricate spatial interdependencies, and the pressing need for more efficient model designs and faster analytical capabilities. Responding to these hurdles, our research unveils the LGL-BCI framework – an avant-garde strategy that capitalizes on a Geometric Deep Learning paradigm for superior EEG data interpretation within the unique confines of non-Euclidean metrics, specifically within the Symmetric Positive Definite (SPD) Manifold arena. The LGL-BCI framework excels in faithfully portraying EEG datasets, adeptly recognizing spatial patterns, and upholding signal consistency. Augmenting this geometric insight, we advocate for a discerning EEG channel filtration mechanism via feature disintegration, aiming to curtail the SPD matrix scale. Our transformation technique is designed to be seamless, adeptly transitioning SPD structures into their tangent dimensions, streamlining computational demands and amplifying inference rapidity. Thorough assessments and practical showcases attest to LGL-BCI's preeminence in terms of precision and agility over prevailing benchmarks. This investigation illuminates the transformative potential of geometric deep learning to elevate MI-BCI capabilities, delivering unparalleled efficacy in tandem with optimized resource deployment. Notably, our efficiency benchmarks, gauged against two eminent EEG repositories, have showcased remarkable enhancements over existing top-performing techniques.

REFERENCES

[1] H. Yuan and B. He, "Brain–computer interfaces using sensorimotor rhythms: current state and future perspectives," *IEEE Transactions on Biomedical Engineering*, vol. 61, no. 5, pp. 1425–1435, 2014.

[2] A. Palumbo, V. Gramigna, B. Calabrese, and N. Ielpo, "Motor-imagery eeg-based bcis in wheelchair movement and control: A systematic literature review," *Sensors*, vol. 21, no. 18, p. 6285, 2021.

[3] A. M. Roy, "A multi-scale fusion cnn model based on adaptive transfer learning for multi-class mi-classification in bci system," *BioRxiv*, pp. 2022–03, 2022.

[4] M. N. Anastasiou, M. Christodoulakis, E. S. Papathanasiou, S. S. Papacostas, A. Hadjipapas, and G. D. Mitsis, "Graph theoretical characteristics of eeg-based functional brain networks in patients with epilepsy: The effect of reference choice and volume conduction," *Frontiers in Neuroscience*, vol. 13, p. 221, 2019.

[5] A. Anzolin, P. Presti, F. Van de Steen, L. Astolfi, S. Haufe, and D. Marinazzo, "Effect of head volume conduction on directed connectivity estimated between reconstructed eeg sources," *BioRxiv*, p. 251223, 2018.

[6] N.-D. Mai, B.-G. Lee, and W.-Y. Chung, "Affective computing on machine learning-based emotion recognition using a self-made eeg device," *Sensors*, vol. 21, no. 15, p. 5135, 2021.

[7] J. Lu, Y. Tian, S. Wang, M. Sheng, and X. Zheng, "Pearnet: A pearson correlation-based graph attention network for sleep stage recognition," in *2022 IEEE 9th International Conference on Data Science and Advanced Analytics (DSAA)*. IEEE, 2022, pp. 1–8.

[8] C. Ju and C. Guan, "Tensor-cspnet: A novel geometric deep learning framework for motor imagery classification," *IEEE Transactions on Neural Networks and Learning Systems*, 2022.

[9] M. Congedo, A. Barachant, and R. Bhatia, "Riemannian geometry for eeg-based brain-computer interfaces: a primer and a review," *Brain-Computer Interfaces*, vol. 4, no. 3, pp. 155–174, 2017.

[10] P. Autthasan, R. Chaisaen, T. Sudhawiyangkul, P. Rangpong, S. Kitathaveephong, N. Dilokthanakul, G. Bhakdisongkham, H. Phan, C. Guan, and T. Wilaiprasitporn, "Min2net: End-to-end multi-task learning for subject-independent motor imagery eeg classification," *IEEE Transactions on Biomedical Engineering*, vol. 69, no. 6, pp. 2105–2118, 2021.

[11] X. Xie, Z. L. Yu, H. Lu, Z. Gu, and Y. Li, "Motor imagery classification based on bilinear sub-manifold learning of symmetric positive-definite matrices," *IEEE Transactions on Neural Systems and Rehabilitation Engineering*, vol. 25, no. 6, pp. 504–516, 2016.

[12] M.-C. Corsi, S. Chevallier, F. D. V. Fallani, and F. Yger, "Functional connectivity ensemble method to enhance bci performance (fucone)," *IEEE Transactions on Biomedical Engineering*, vol. 69, no. 9, pp. 2826–2838, 2022.

[13] F. Lotte, L. Bougrain, A. Cichocki, M. Clerc, M. Congedo, A. Rakotomamonjy, and F. Yger, "A review of classification algorithms for eeg-based brain–computer interfaces: a 10 year update," *Journal of neural engineering*, vol. 15, no. 3, p. 031005, 2018.

[14] Z. Lin, "Riemannian geometry of symmetric positive definite matrices via cholesky decomposition," *SIAM Journal on Matrix Analysis and Applications*, vol. 40, no. 4, pp. 1353–1370, 2019.

[15] Z. J. Koles, M. S. Lazar, and S. Z. Zhou, "Spatial patterns underlying population differences in the background eeg," *Brain topography*, vol. 2, no. 4, pp. 275–284, 1990.

[16] H. Lu, H.-L. Eng, C. Guan, K. N. Plataniotis, and A. N. Venetsanopoulos, "Regularized common spatial pattern with aggregation for eeg classification in small-sample setting," *IEEE transactions on Biomedical Engineering*, vol. 57, no. 12, pp. 2936–2946, 2010.

[17] F. Lotte and C. Guan, "Regularizing common spatial patterns to improve bci designs: unified theory and new algorithms," *IEEE Transactions on biomedical Engineering*, vol. 58, no. 2, pp. 355–362, 2010.

[18] V. J. Lawhern, A. J. Solon, N. R. Waytowich, S. M. Gordon, C. P. Hung, and B. J. Lance, "Eegnet: a compact convolutional neural network for eeg-based brain–computer interfaces," *Journal of neural engineering*, vol. 15, no. 5, p. 056013, 2018.

[19] S. Sakhavi, C. Guan, and S. Yan, "Learning temporal information for brain–computer interface using convolutional neural networks," *IEEE transactions on neural networks and learning systems*, vol. 29, no. 11, pp. 5619–5629, 2018.

[20] J.-S. Bang, M.-H. Lee, S. Fazli, C. Guan, and S.-W. Lee, "Spatio-spectral feature representation for motor imagery classification using convolutional neural networks," *IEEE Transactions on Neural Networks and Learning Systems*, vol. 33, no. 7, pp. 3038–3049, 2021.

[21] J. R. Stieger, S. A. Engel, D. Suma, and B. He, "Benefits of deep learning in classification of continuous noninvasive brain–computer interface control," *Journal of neural engineering*, vol. 18, no. 4, p. 046082, 2021.

[22] J. Bruna and S. Mallat, "Invariant scattering convolution networks," *IEEE transactions on pattern analysis and machine intelligence*, vol. 35, no. 8, pp. 1872–1886, 2013.

[23] Y. LeCun, Y. Bengio, and G. Hinton, "Deep learning," *nature*, vol. 521, no. 7553, pp. 436–444, 2015.

[24] M. M. Bronstein, J. Bruna, Y. LeCun, A. Szlam, and P. Vandergheynst, "Geometric deep learning: going beyond euclidean data," *IEEE Signal Processing Magazine*, vol. 34, no. 4, pp. 18–42, 2017.

[25] Z. Huang and L. Van Gool, "A riemannian network for spd matrix learning," in *Proceedings of the AAAI conference on artificial intelligence*, vol. 31, no. 1, 2017.

[26] Y.-T. Pan, J.-L. Chou, and C.-S. Wei, "Matt: a manifold attention network for eeg decoding," *Advances in Neural Information Processing Systems*, vol. 35, pp. 31116–31129, 2022.

[27] F. Yger, M. Berar, and F. Lotte, "Riemannian approaches in brain–computer interfaces: review," *IEEE Transactions on Neural Systems and Rehabilitation Engineering*, vol. 25, no. 10, pp. 1753–1762, 2016.

[28] C. Ju and C. Guan, "Graph neural networks on spd manifolds for motor imagery classification: A perspective from the time-frequency analysis," *arXiv preprint arXiv:2211.02641*, 2022.

[29] K. K. Ang, Z. Y. Chin, H. Zhang, and C. Guan, "Filter bank common spatial pattern (fbcsp) in brain–computer interface," in *2008 IEEE international joint conference on neural networks (IEEE world congress on computational intelligence)*. IEEE, 2008, pp. 2390–2397.

[30] D. Gabor, "Theory of communication. part 1: The analysis of information," *Journal of the Institution of Electrical Engineers-part III: radio and communication engineering*, vol. 93, no. 26, pp. 429–441, 1946.

[31] Z. Abdi Alkareem Alyasser, O. A. Alomari, M. A. Al-Betar, M. A. Awadallah, K. Hameed Abdulkareem, M. Abed Mohammed, S. Kadry, V. Rajinikanth, S. Rho *et al.*, "Eeg channel selection using multiobjective cuckoo search for person identification as protection system in healthcare applications," *Computational Intelligence and Neuroscience*, vol. 2022, 2022.

[32] T. Strypsteen and A. Bertrand, "End-to-end learnable eeg channel selection for deep neural networks with gumbel-softmax," *Journal of Neural Engineering*, vol. 18, no. 4, p. 04609, 2021.

[33] W. Gao, Z. Ma, W. Gan, and S. Liu, "Dimensionality reduction of spd data based on riemannian manifold tangent spaces and isometry," *Entropy*, vol. 23, no. 9, p. 1117, 2021.

[34] X. Pennec, P. Fillard, and N. Ayache, "A riemannian framework for tensor computing," *International Journal of computer vision*, vol. 66, pp. 41–66, 2006.

[35] M. S. Bartlett, "Multivariate analysis," *Supplement to the journal of the royal statistical society*, vol. 9, no. 2, pp. 176–197, 1947.

[36] A. Vaswani, N. Shazeer, N. Parmar, J. Uszkoreit, L. Jones, A. N. Gomez, Ł. Kaiser, and I. Polosukhin, "Attention is all you need," *Advances in neural information processing systems*, vol. 30, 2017.

[37] J. Hu, L. Shen, and G. Sun, "Squeeze-and-excitation networks," in *Proceedings of the IEEE conference on computer vision and pattern recognition*, 2018, pp. 7132–7141.

[38] M.-H. Lee, O.-Y. Kwon, Y.-J. Kim, H.-K. Kim, Y.-E. Lee, J. Williamson, S. Fazli, and S.-W. Lee, "Eeg dataset and openbmi toolbox for three bci paradigms: An investigation into bci illiteracy," *GigaScience*, vol. 8, no. 5, p. giz002, 2019.

[39] M. Tangermann, K.-R. Müller, A. Aertsen, N. Birbaumer, C. Braun, C. Brunner, R. Leeb, C. Mehring, K. J. Miller, G. Mueller-Putz *et al.*, "Review of the bci competition iv," *Frontiers in neuroscience*, p. 55, 2012.

[40] G. Tevet, S. Raab, B. Gordon, Y. Shafir, D. Cohen-Or, and A. H. Bermano, "Human motion diffusion model," *arXiv preprint arXiv:2209.14916*, 2022.

[41] J. Lin, C. Gan, and S. Han, "Temporal shift module for efficient video understanding. corr abs/1811.08383 (2018)," 1811.

[42] C. Ju and C. Guan, "Graph neural networks on spd manifolds for motor imagery classification: A perspective from the time-frequency analysis," *IEEE Transactions on Neural Networks and Learning Systems*, 2023.

[43] Y. Liu, H. Shao, and B. Bai, "A novel convolutional neural network architecture with a continuous symmetry," *arXiv preprint arXiv:2308.01621*, 2023.

[44] R. Mane, E. Chew, K. Chua, K. K. Ang, N. Robinson, A. P. Vinod, S.-W. Lee, and C. Guan, "Fbcnet: A multi-view convolutional neural network

for brain-computer interface,” *arXiv preprint arXiv:2104.01233*, 2021.

[45] G. Pfurtscheller, C. Brunner, A. Schlogl, and F. L. Da Silva, “Mu rhythm (de) synchronization and eeg single-trial classification of different motor imagery tasks,” *NeuroImage*, vol. 31, no. 1, pp. 153–159, 2006.

[46] A. Aldridge, E. Barnes, C. L. Bethel, D. W. Carruth, M. Kocturova, M. Pleva, and J. Juhar, “Accessible electroencephalograms (eegs): A comparative review with openbci’s ultracortex mark iv headset,” in *2019 29th International Conference Radioelektronika (RADIOELEKTRONIKA)*. IEEE, 2019, pp. 1–6.